Energy & Environmental Science

PAPER

View Article Online
View Journal | View Issue

Cite this: *Energy Environ. Sci.*, 2018, **11**, 1307

Solution-printable fullerene/TiS_2 organic/inorganic hybrids for high-performance flexible n-type thermoelectrics†

Liming Wang,[a] Zimeng Zhang,[a] Linxiao Geng,[b] Tianyu Yuan,[c] Yuchen Liu,[a] Juchen Guo,[b] Lei Fang,[c] Jingjing Qiu[d] and Shiren Wang*[a]

Solution-printable and flexible thermoelectric materials have attracted great attention because of their scalable processability and great potential for powering flexible electronics, but it is challenging to integrate mechanical flexibility, solution-printability and outstanding thermoelectric properties together. In particular, such an n-type thermoelectric material is highly sought after. In this paper, 2D TiS_2 nanosheets were exfoliated from layered polycrystalline powders, and then assembled with C_{60} nanoparticles, resulting in a new class of flexible n-type thermoelectric materials *via* a concurrent enhancement in the power factor and a reduction in thermal conductivity. The resultant C_{60}/TiS_2 hybrid films show a $ZT \sim 0.3$ at 400 K, far superior to the state-of-the-art solution-printable and flexible n-type thermoelectric materials. In particular, such a thermoelectric property rivals that of single-crystal TiS_2-based thermoelectric materials, which are expensive, difficult to synthesize, and unsuitable for solution printing. A solution of the C_{60}/TiS_2 hybrid was also used as an ink for printing large-area flexible and spatial thermoelectric devices. An outstanding output power of 1.68 W m^{-2} was generated at a temperature gradient of 20 K. This work paves the way for flexible, solution-printable, high-performance thermoelectric materials for flexible electronics.

Received 22nd December 2017,
Accepted 12th March 2018

DOI: 10.1039/c7ee03617e

rsc.li/ees

Broader context

More than half of industrial energy is lost as waste heat, and thus it is critical to recycle waste heat for efficient energy utilization. Thermoelectrics involving the conversion between heat and electricity can recycle such wasted heat in a safe and environmentally friendly manner. Thermoelectrics can also produce clean energy by harvesting thermal energy from sustainable resources, and facilitate water reuse for global sustainability. They also have great potential for high-precision thermal sensors and non-invasive or minimally-invasive therapy. In contrast to conventional rigid thermoelectrics, flexible thermoelectrics show a huge advantage of easy integration in versatile formats but are limited by their inferior thermoelectric properties. In this paper, we demonstrate n-type fullerene/TiS_2 organic/inorganic hybrid films which integrate mechanical flexibility, solution-printability and outstanding thermoelectric properties together. Our work opens a new door for utilizing flexible thermoelectric materials in the field of stretchable electronics, flexible power generators, tunable water-reuse systems, and adaptable sensors.

Introduction

The thermoelectric effect, which involves direct conversion between thermal energy and electrical energy without moving parts or hazardous working fluids, has attracted increasing attention in terms of sustainability.[1–5] In particular, thermoelectric materials can harvest body heat to supply power to wearable electronics. Flexible thermoelectric materials without toxic or rare elements are extremely attractive and preferred, especially those that are solution-printable. The efficiency of energy conversion is determined by the figure of merit (ZT) of materials, defined as $ZT = S^2\sigma T/\kappa$, where S is the Seebeck coefficient, σ is the electrical conductivity, κ is the thermal conductivity, and T is the absolute temperature. Rigid inorganic materials such as Bi_2Te_3 demonstrate high ZT, but their lack of flexibility hinders their potential for wearable power sources. Alternatively, organic thermoelectric materials have received great attention because of their flexibility and recent break-throughs in their

[a] Department of Industrial and Systems Engineering, Texas A&M University, College Station, TX 77843, USA. E-mail: s.wang@tamu.edu
[b] Department of Chemical and Environmental Engineering, University of California, Riverside, CA 92521, USA
[c] Department of Chemistry, Texas A&M University, College Station, TX 77843, USA
[d] Department of Mechanical Engineering, Texas Tech University, Lubbock, TX77409, USA

† Electronic supplementary information (ESI) available. See DOI: 10.1039/c7ee03617e

thermoelectric properties.[6–10] For example, solution-processed p-type poly(3,4-ethylenedioxythiophene) (PEDOT) based films demonstrated outstanding thermoelectric properties with $ZT > 0.25$.[6,7] Unfortunately, the development of n-type organic thermoelectric materials significantly lags behind that of their p-type counterparts in terms of low electron transport properties and poor stability.[11–14]

Organic/inorganic hybrids have emerged as a new class of flexible n-type thermoelectric materials; in particular, organic material-intercalated transition metal dichalcogenides (TMD) have great potential for flexible air-stable n-type thermoelectrics. TiS_2, a type of 2D transition metal dichalcogenide (TMD), is a very promising candidate for n-type thermoelectrics due to advantages including it being environmentally benign, chemical stability, mechanical flexibility and it being composed of the earth-abundant elements Ti and S.[15–18] Furthermore, a TiS_2 single crystal was reported to have a very high power factor (PF, $S^2\sigma$) of 3710 μW m^{-1} K^{-2} even at room temperature, which rivaled those of the state-of-the-art Bi_2Te_3 alloys.[19] However, its ZT was rather low, only 0.16 at 300 K because of the relatively large thermal conductivity (6.8 W m^{-1} K^{-1}).[19,20] Therefore, an important strategy is to reduce thermal conductivity and maintain a high power factor for a higher ZT. In particular, reducing the lattice thermal conductivity, which mainly contributes to the total high thermal conductivity, is an effective way of improving the ZT of TiS_2. Recently, Koumoto *et al.* used organic solvent molecules to intercalate TiS_2 single crystal and achieved an ultralow in-plane lattice thermal conductivity of 0.12 W m^{-1} K^{-1}, resulting in a ZT value of ∼0.2 at room temperature.[15] But intercalation of these molecules also led to significant decrease of the Seebeck coefficient and thus the power factor, as shown in Fig. 1a.[15,17,21] In addition, it is almost impossible to grow large-size TiS_2 single crystals for scalable production (for example, the current single crystal TiS_2 is usually around 4 mm × 4 mm). In comparison, polycrystalline TiS_2 powders are suitable for mass-production and scalable solution processing. However, the thermoelectric properties of polycrystalline TiS_2 powders are much poorer, only 0.09 (ZT) at room temperature.[17] It will be of great interest to tune the polycrystalline TiS_2 powders so that their thermoelectric properties are comparable to the single crystal TiS_2.

The inclusion of nanostructures is a very promising strategy to improve the thermoelectric properties of polycrystalline TiS_2 films, which can greatly reduce the thermal conductivity *via* phonon scattering while slightly affecting the electron transport.[22,23] Significant progress has been made in thermoelectric materials *via* nanostructure-induced phonon scattering, such as BiSbTe alloys and PbTe.[24–29] Recent attempts have indicated that organic/inorganic hybrid nanostructures could demonstrate significantly-improved thermoelectric properties by reduction of thermal conductivity, such as graphene/skutterudite composites and carbon nanotubes/Cu_2Se composites.[30,31] Carbon nanocrystals, C_{60}, with an extremely high Seebeck coefficient (−2000 μV K^{-1}) and low thermal conductivity (0.16 W m^{-1} K^{-1}) at room temperature[32–34] could be an ideal nanofiller to reduce the thermal conductivity of TiS_2 2D crystals while maintaining their high Seebeck coefficient and thus high power factor. However, to the best of our knowledge, no attempt has been reported to design and prepare such a novel C_{60}/TiS_2 hybrid nanostructure, and there is a lack of fundamental understanding about the assembly, characterization, and thermoelectric properties of such novel hybrid nanostructures.

In this paper, we present the liquid assembly of 0D C_{60} nanoparticles onto 2D TiS_2 nanosheets to synthesize novel organic/inorganic heterostructures and study the thermoelectric properties of the as-produced hybrids. Tailoring C_{60} nanoparticles increased the power factor of TiS_2 by >1.5-fold and also significantly decreased the thermal conductivity through phonon scattering (Fig. 1a). As a result, the thermoelectric property of the as-assembled C_{60}/TiS_2 hybrid films could rival that of the state-of-the-art TiS_2 single crystals.[15,21] The as-produced novel hybrids can also be dispersed in solvents and used as an ink for printing large-area and flexible thermoelectric devices. A power density of 1.68 W m^{-2} for the printed device was achieved

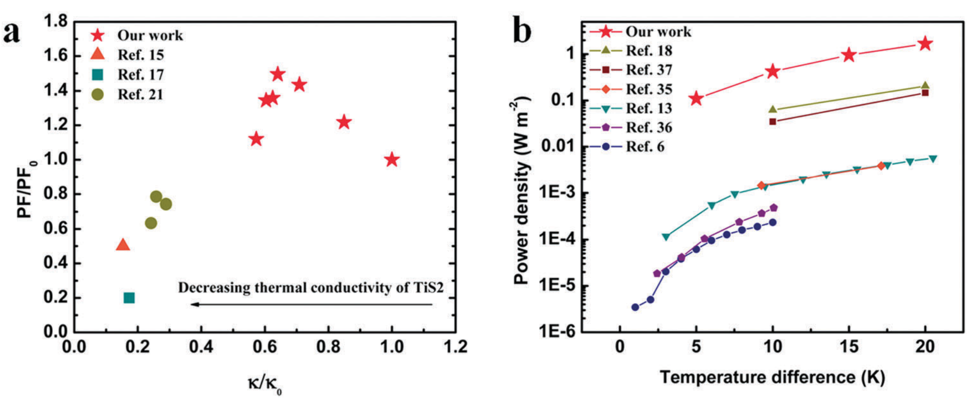

Fig. 1 (a) The variation of the power factor on decreasing the thermal conductivity of TiS_2. PF_0 and κ_0 are the power factor and thermal conductivity of TiS_2, respectively. Typically, a decrease in thermal conductivity accompanies a reduction in the power factor.[15,17,21] In contrast, our work demonstrates a simultaneous decrease in thermal conductivity and enhancement in the power factor. (b) Comparisons of power density between the thermoelectric device of our work and reported thermoelectric devices based on organic materials or organic/inorganic composites.[6,13,18,35–37] The temperature differences are within 20 K which is easy to realize in a natural setting.

under a temperature gradient of 20 K (ΔT = 20), which was much higher than that of the reported thermoelectric devices based on organic materials or organic/inorganic composites (Fig. 1b).[6,13,18,35–37] Integration of solution-printability, air stability, and flexibility makes the as-assembled C_{60}/TiS_2 hybrids a new class of flexible high-performance thermoelectric materials for flexible electronics.

Results and discussion

Fabrication of C_{60}/TiS_2 hybrid films

Because of the significant solubility difference of C_{60} and TiS_2, directly mixing them in a common solvent is not possible for the assembly of C_{60}/TiS_2 hybrids. Hence, a facile liquid process *via* solvent transfer and surface deposition is developed to solve this problem, as illustrated in Fig. 2. In a typical procedure, TiS_2 nanosheets were dispersed into isopropyl alcohol (IPA), while a small amount of C_{60}/toluene solution was gradually injected into the TiS_2/IPA solution under the assistance of bath sonication. Toluene and IPA are miscible, while the solubility of C_{60} in IPA is very low. Therefore, C_{60} nanoparticles gradually precipitated in IPA and preferably deposited on the hydrophobic surface of the TiS_2 nanosheets because of the van der Waals interaction.

The composition and morphology of the pristine TiS_2 powders were confirmed by the X-ray diffraction (XRD) and scanning electron microscopy (SEM) results, as shown in Fig. S1 and S2 (ESI†). Exfoliated TiS_2 nanosheets were also characterized by using an atomic force microscope (AFM) (Fig. 3a and Fig. S3, ESI†), and the cross-section analysis was carried out. The statistical distribution of the exfoliated TiS_2 nanosheet thickness is shown in Fig. 3b, and most of them are less than 2 nm-thick, indicating single-layer or two-layer nanosheets. The transmission electron microscope (TEM) characterization indicated that the as-exfoliated TiS_2 nanosheets showed a smooth and clean surface (Fig. 3c). In contrast, numerous small C_{60} nanoparticles were clearly observed on the surface of the TiS_2 nanosheets for the C_{60}-assembled TiS_2 hybrids as shown in Fig. 3d. The size of most C_{60} aggregates on the TiS_2 nanosheets was around 5 nm. The C_{60}/TiS_2 suspension was very stable for more than one month, and can be used as an ink to print large-area films. The as-produced freestanding and flexible C_{60}/TiS_2 hybrid film is shown in Fig. 3e. The cross-section of such a hybrid film was also characterized by SEM, clearly indicating the layered structure (Fig. 3f). The as-produced C_{60}/TiS_2 hybrid film was also characterized by Raman spectroscopy. As shown in Fig. 3g, a peak at 334 cm^{-1} was observed in the spectra of both the TiS_2 film and hybrid film. This low-frequency band was assigned to the A_{1g} mode, corresponding to the vibration of sulfur atoms perpendicular to the sulfur layer. The features of the spectra are similar to those of 1T-TiS_2 (CdI_2 type structure).[38] Several characteristic peaks were observed in the Raman spectrum of C_{60}. In the Raman spectrum of the hybrid film, both characteristic peaks of C_{60} and TiS_2 were observed, further confirming the intercalation of C_{60} in the TiS_2 layers. The XRD characterization results of the re-stacked TiS_2 film and the C_{60}/TiS_2 nanosheet hybrid films are shown in Fig. 3i. All the characteristic peaks observed in the XRD patterns are consistent with those in the reference PDF# 15-853.[39,40] The (001) peak of the re-stacked TiS_2 film slightly shifted to a lower degree compared to the pristine TiS_2 powders, indicating the increase of the layer spacing. For the hybrid films, the (001) peak further shifted to a lower degree with increasing C_{60} fractions. Obviously, the enlarged interlayer spacing was induced by the intercalation of C_{60} nanoparticles. The XRD peaks of C_{60} were not found for

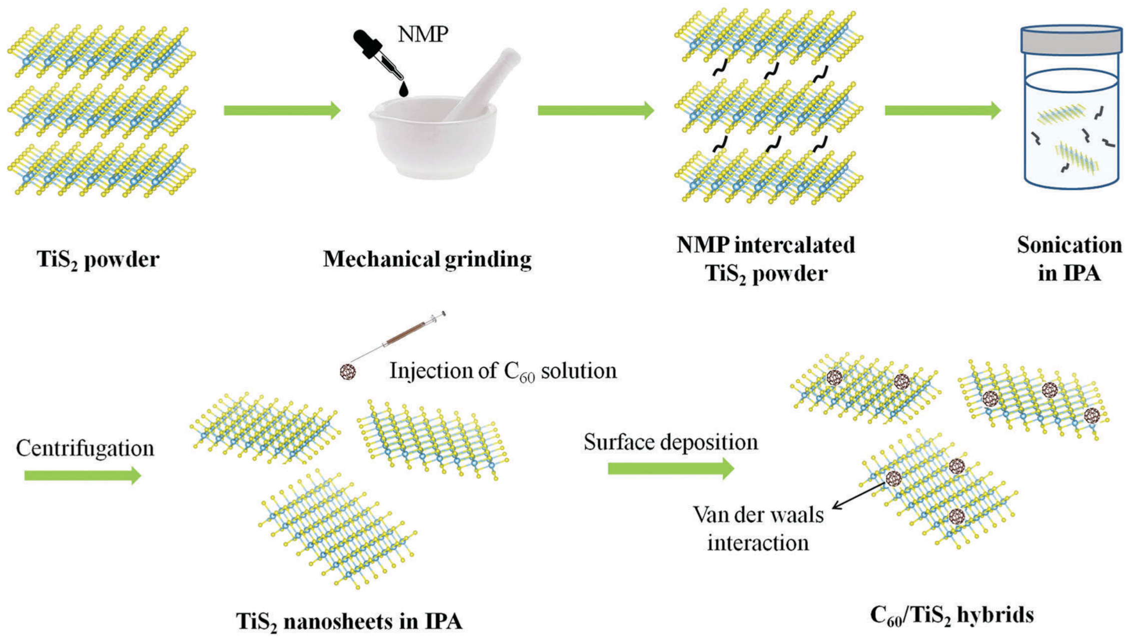

Fig. 2 Scheme of fabricating C_{60}/TiS_2 nanosheet hybrids by a liquid process.

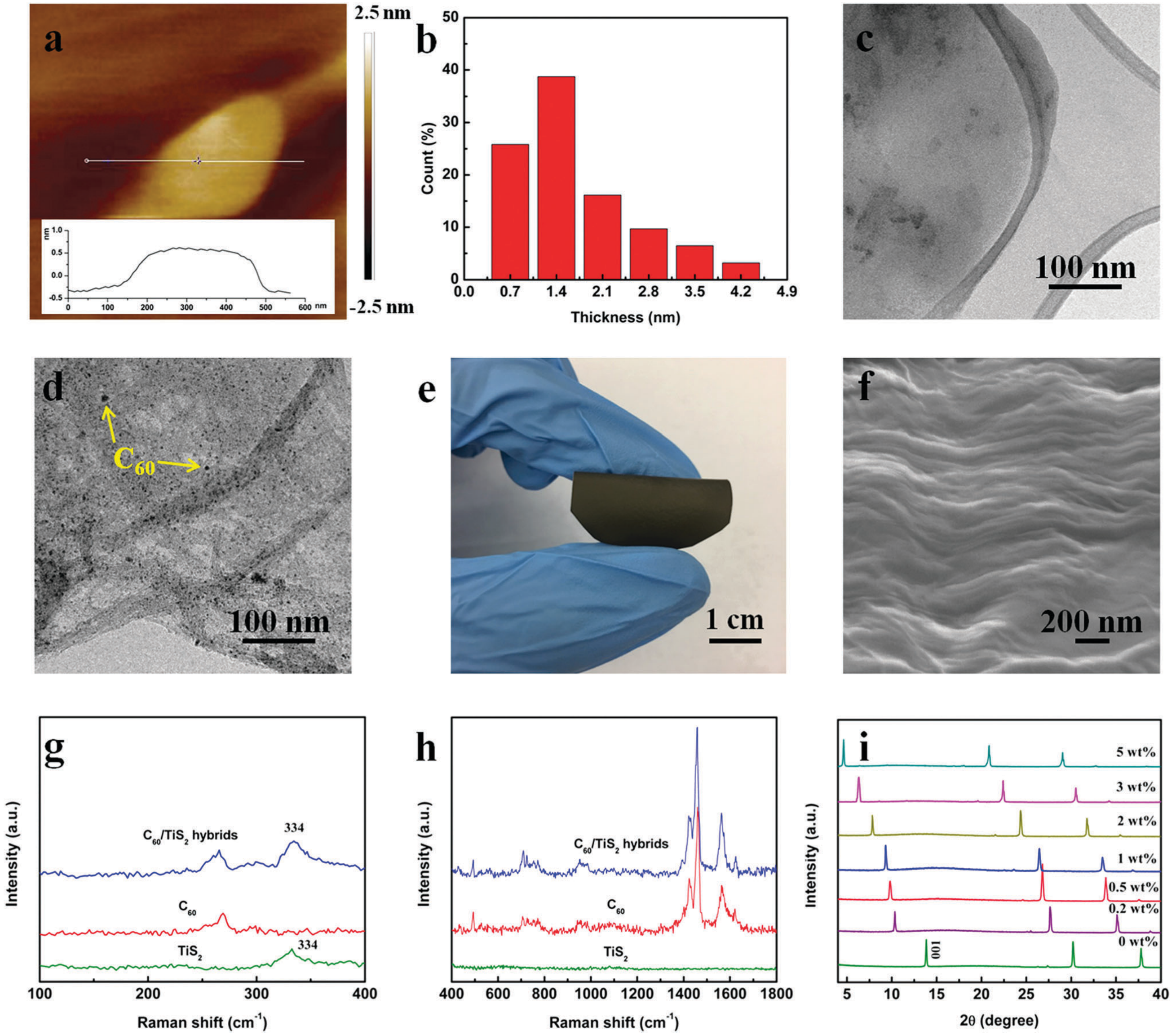

Fig. 3 Characterization of the synthesized C_{60}/TiS_2 nanosheet hybrid films. (a) Typical AFM image of an exfoliated TiS_2 nanosheet. (b) The thickness distribution of exfoliated TiS_2 nanosheets. (c) TEM image of TiS_2 nanosheets. (d) TEM image of 1 wt% C_{60}/TiS_2 nanosheet hybrids. (e) Digital image of the fabricated flexible C_{60}/TiS_2 nanosheet (1 wt% C_{60} content) hybrid film in a large area of 3 cm × 3 cm. (f) Cross-sectional SEM image of the fabricated 1 wt% C_{60}/TiS_2 nanosheet hybrid film. (g and h) Raman spectra of the TiS_2 film, C_{60} powders, and 1 wt% C_{60}/TiS_2 nanosheet hybrid film. (i) XRD patterns of the TiS_2 film and C_{60}/TiS_2 nanosheet hybrid films with different C_{60} contents.

the hybrid samples, which was mainly due to the very low C_{60} amount. Similar phenomena were also reported in the previous literature.[41,42]

Thermoelectric performance

The electrical conductivity and Seebeck coefficient of the prepared films were characterized as a function of the C_{60} fraction in the in-plane direction at room temperature and the results are shown in Fig. 4a and b. The re-stacked TiS_2 films showed an electrical conductivity of $\sim$480 S cm^{-1} and a Seebeck coefficient of ~ -75 μV K^{-1}. After assembling the C_{60} nanoparticles on the surface of the TiS_2 nanosheets, the electrical conductivity persistently decreased while the Seebeck coefficient increased with an increasing C_{60} amount. When the C_{60} amount was 1 wt%, the Seebeck coefficient of the hybrid films reached -101 μV K^{-1}. On further increase of the C_{60} amount, the enhancement in the Seebeck coefficient was very slight. This may be caused by the aggregation of C_{60}. Because of the limited surface on the TiS_2 nanosheets, continuously adding C_{60} above 1 wt% could force them to aggregate to form larger clusters, as indicated by the XRD results in Fig. 3i. The carrier concentration of the fabricated films was measured and is shown in Fig. S8 (ESI†), and decreased with increasing C_{60} content. The influence of the varied carrier concentration on the Seebeck coefficient was evaluated by the Pisarenko plot,[43] as shown in Fig. S9 (ESI†). Our experimental results of the Seebeck coefficient for the hybrid

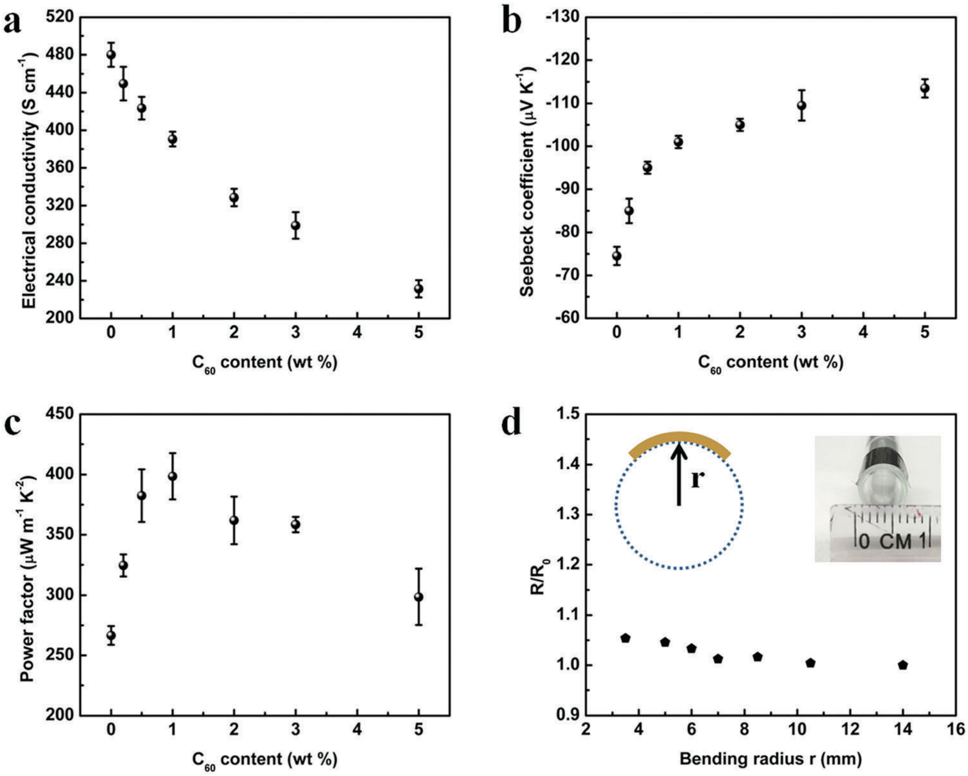

Fig. 4 In-plane thermoelectric properties of the fabricated TiS_2 film and C_{60}/TiS_2 nanosheet hybrid films as a function of C_{60} content, and the air stability of the hybrid film. (a) Electrical conductivity. (b) Seebeck coefficient. (c) Power factor. (d) The resistance R of the 1 wt% C_{60}/TiS_2 hybrid film as a function of the bending radius r, where R_0 is the resistance before bending. The resistance was measured by attaching the hybrid film to glass tubes with different diameters.

films were larger than the calculated values, indicating that the reduction of carrier concentration only partially contributed to the enhancement of the Seebeck coefficient. Some other factors, such as C_{60} components and interfacial scattering, could also significantly contribute to the enhancement of the Seebeck coefficient.[44] A maximum power factor of as high as ~400 μW m^{-1} K^{-2} was observed in the C_{60}/TiS_2 hybrid films at 1 wt% C_{60}, which is much higher than that of the re-stacked TiS_2 films, and previously reported n-type TMD polycrystalline films (see Table S2, ESI†).[17,18,45,46] These results have confirmed that it is feasible to maintain or even enhance the high thermoelectric power factor of TiS_2 by C_{60} intercalation. The as-fabricated C_{60}/TiS_2 hybrid film also demonstrates a good flexibility, as shown in Fig. 4d. The increase of electrical resistance for the 1 wt% C_{60}/TiS_2 hybrid film was within 5% even at a bending radius of 3.5 mm. The stability of the prepared C_{60}/TiS_2 hybrid film was also investigated. As illustrated in Fig. S10 (ESI†), the hybrid film demonstrated negligible changes in both the electrical conductivity and Seebeck coefficient during the testing.

More impressively, inclusion of C_{60} nanoparticles onto the surface of TiS_2 nanosheets can also significantly decrease the thermal conductivity (especially the lattice thermal conductivity) of TiS_2 because of the phonon scattering. The in-plane thermal conductivity was characterized by a laser flash method, and is shown in Fig. 5a. When the C_{60} content was increased to 1 wt% in the hybrid film, the thermal conductivity dramatically decreased from 0.96 W m^{-1} K^{-1} to 0.61 W m^{-1} K^{-1}, an almost 36% reduction. However, further increasing the C_{60} content only led to a slight reduction in thermal conductivity. The lattice thermal conductivity (κ_l) can be calculated by subtracting the carrier part κ_e from the total κ, where κ_e is calculated by the Wiedemann–Franz law ($\kappa_e = L_0\sigma T$). L_0 is the Lorentz number and can be given as follows,

$$L_0 = \left(\frac{k_B}{e}\right)^2 \left(\frac{(r+7/2)F_{(r+5/2)}(\eta)}{(r+3/2)F_{(r+1/2)}(\eta)} - \left[\frac{(r+5/2)F_{(r+3/2)}(\eta)}{(r+3/2)F_{(r+1/2)}(\eta)}\right]^2\right), \tag{1}$$

where k_B is the Boltzmann constant, e is the electron charge, r is the scattering factor, and η is the reduced Fermi energy. The dominant scattering mechanism of TiS_2 is acoustic phonon scattering, so $r = -1/2$.[15] The reduced Fermi energy η should be derived from the measured Seebeck coefficients,

$$S = \pm\frac{k_B}{e}\left(\frac{(r+5/2)F_{(r+3/2)}(\eta)}{(r+3/2)F_{(r+1/2)}(\eta)} - \eta\right), \tag{2}$$

where $F_n(\eta)$ is the nth-order Fermi integral,

$$F_n(\eta) = \int_0^\infty \frac{\chi^n}{1+e^{\chi-\eta}}\mathrm{d}\chi. \tag{3}$$

The calculated lattice thermal conductivities are shown in Fig. 5b. Similar to the trend of total thermal conductivity, the

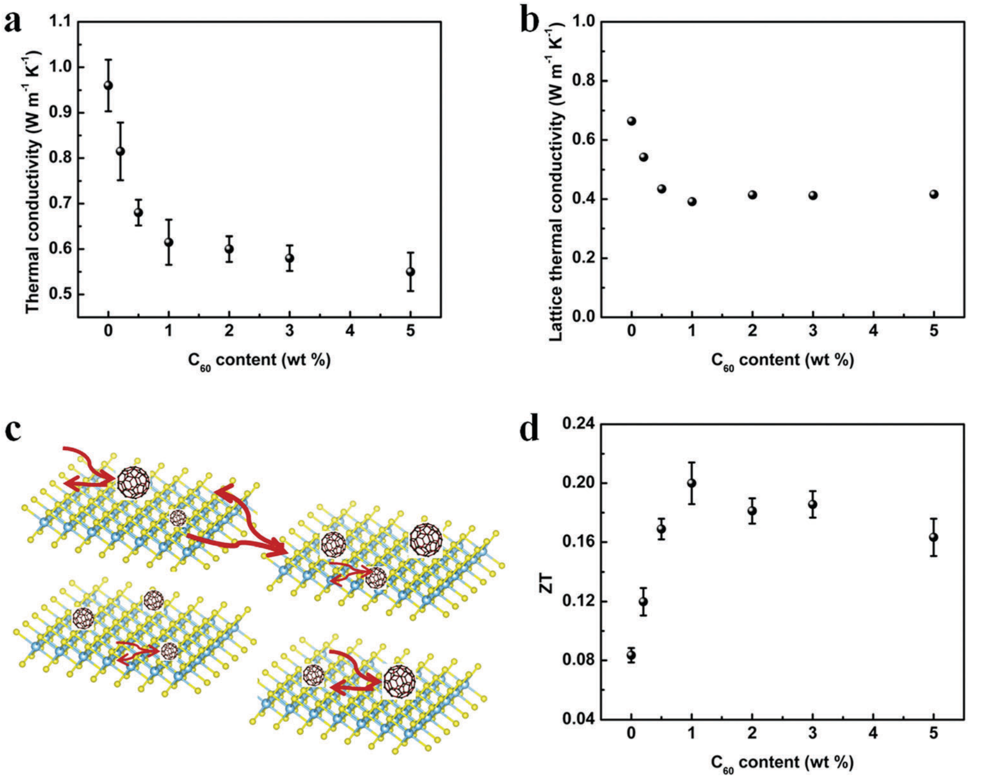

Fig. 5 In-plane thermoelectric properties of the fabricated TiS_2 film and C_{60}/TiS_2 nanosheet hybrid films as a function of C_{60} content. (a) Thermal conductivity. (b) Lattice thermal conductivity. (c) Schematic illustration of phonon scattering in the C_{60}/TiS_2 nanosheet hybrid films. (d) *ZT versus* C_{60} fraction.

lattice thermal conductivity of the hybrid film rapidly decreased to 0.39 W m^{-1} K^{-1} at 1 wt% C_{60}, and then decreased very slightly with increasing C_{60} content. The thermal conductivity of the TiS_2 single crystal was as high as ~6.8 W m^{-1} K^{-1}, while the thermal conductivity of the sintered TiS_2 polycrystals was reported to be ~3.4 W m^{-1} K^{-1}.[19,47,48] In comparison, the thermal conductivity of the as-fabricated C_{60}/TiS_2 hybrid films was very low. Previous work showed that the ultralow in-plane thermal conductivity of ~0.7 W m^{-1} K^{-1} and the lattice thermal conductivity of ~0.12 W m^{-1} K^{-1} can be achieved by using organic molecules to intercalate the TiS_2 single crystal.[15] In this work, the significant reduction of thermal conductivity can be attributed to the phonon scattering induced by the grain boundary between TiS_2 nanosheets and C_{60} nanoparticles. As illustrated in Fig. 5c, the grain boundary of TiS_2 nanosheets can effectively scatter the long-wavelength phonons. The smaller-size C_{60} nanoparticles preferably scatter the mid-wavelength and short-wavelength phonons. As mentioned above, there was a limited surface area to assemble the C_{60} nanoparticles on each TiS_2 nanosheet. Therefore, a high fraction of C_{60} nanoparticles tended to aggregate and thus cannot effectively increase the number of phonon scatter centers, resulting in a slow decrease of thermal conductivity. Based on the experimental measurements, the *ZT* value (~300 K) was as high as 0.2 for the 1 wt% C_{60}/TiS_2 nanosheet hybrid films, which is comparable to the state-of-the-art TiS_2 single crystals.[15,21]

The temperature-dependent thermoelectric properties of the TiS_2 film and the 1 wt% C_{60}/TiS_2 hybrid film are shown in Fig. 6. The electrical conductivities of both the TiS_2 film and the hybrid film decreased with increasing temperature, displaying metallic conductive behavior. This changing trend is consistent with those in recent publications on organic molecule intercalated TiS_2 materials.[15,21] In contrast to the electrical conductivity, the Seebeck coefficients of both the TiS_2 film and the hybrid film increased with increasing temperature. As a result, the power factor of the TiS_2 film stayed stable with increasing temperature while the power factor of the C_{60}/TiS_2 hybrid film decreased slightly with increasing temperature, from ~400 μW m^{-1} K^{-2} at ~300 K to 375 μW m^{-1} K^{-2} at ~400 K. Overall, the C_{60}/TiS_2 hybrid films demonstrated a much larger power factor than the TiS_2 film in the whole temperature range of measurement. The temperature-dependent thermal conductivities including the lattice thermal conductivities of the two films are shown in Fig. 6d. It was clearly observed that assembling C_{60} nanoparticles onto TiS_2 nanosheets greatly decreased both the total thermal conductivity and lattice thermal conductivity of TiS_2. Moreover, the total thermal conductivity of the hybrid film slightly decreased with increasing temperature. As a result, the *ZT* value of the 1 wt% C_{60}/TiS_2 hybrid film increased to 0.3 at 400 K. The thermoelectric properties of the state-of-the-art n-type organic materials and organic/inorganic hybrid materials are summarized in Fig. 6f, including the organic intercalated TMDs,[15,17,21] metal coordination polymers,[13,14] insulating polymer/metal composites,[49] and PEI doped carbon nanotubes.[50] The *ZT* value of the as-prepared C_{60}/TiS_2 polycrystalline flexible films is comparable to that of the

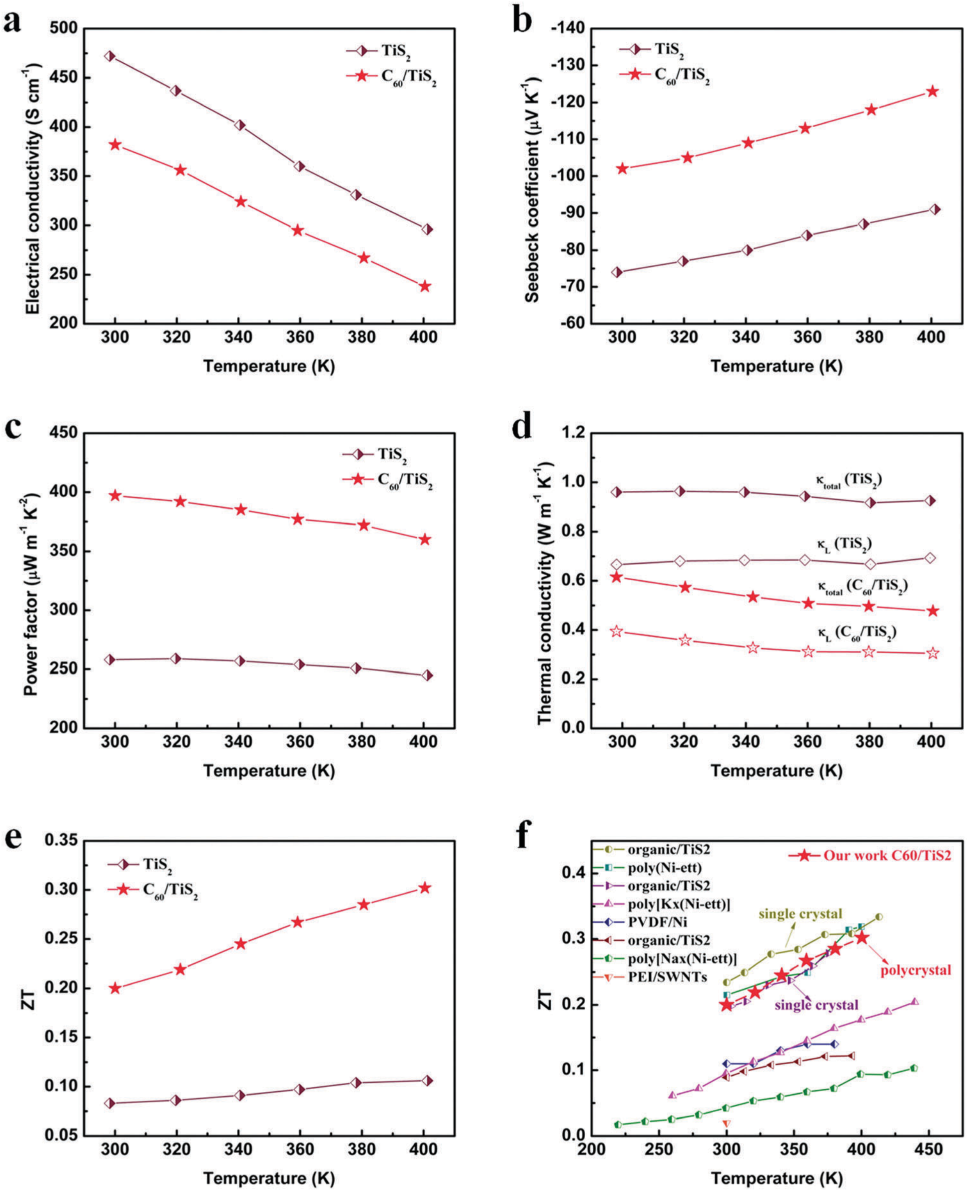

Fig. 6 High-temperature in-plane thermoelectric properties of the fabricated TiS_2 film and the 1 wt% C_{60}/TiS_2 nanosheet hybrid film. (a) Electrical conductivity. (b) Seebeck coefficient. (c) Power factor. (d) Total thermal conductivity and lattice thermal conductivity. (e) *ZT*. (f) Comparisons of *ZT* values for state-of-the-art flexible and printable organic thermoelectrics and organic/inorganic hybrid thermoelectrics.[13–15,17,21,49,50]

single crystal TiS_2 materials, and among the highest for flexible n-type thermoelectric materials.

Device performance

Owing to the good processability, the as-prepared C_{60}/TiS_2 hybrids are suitable for scalable, cost-effective, high-rate and continuous solution processes, and thus it is convenient to fabricate large-area flexible thermoelectric devices by printing techniques such as the roll-to-roll printing reported by our group.[51] A flexible thermoelectric module composed of 4 parallelly connected legs was fabricated using 1 wt% C_{60}/TiS_2 hybrid films as n-type legs while 50 wt% single-walled carbon nanotubes (SWNTs)/PEDOT:PSS hybrid films were used as p-type legs, as shown in Fig. 7b. Each component leg was 10 mm in length, 5 mm in width, and 10 μm in thickness. The electrical resistance of the as-fabricated device was measured to be 16.6 Ω. In principle, the output voltage of the thermoelectric device can be given by $U = E - IR_{in}$, where E is the open-circuit voltage of the device, R_{in} is the resistance of the device, and I is the output current. Hence, the output voltage is inversely proportional to the output current at a certain temperature gradient. As shown in Fig. 7c, the output current–voltage curves were plotted against different temperature gradients by connecting the device with an external load resistance in series. An inverse relationship was observed between the current and voltage, and the output voltages increase with the increasing temperature difference, reaching

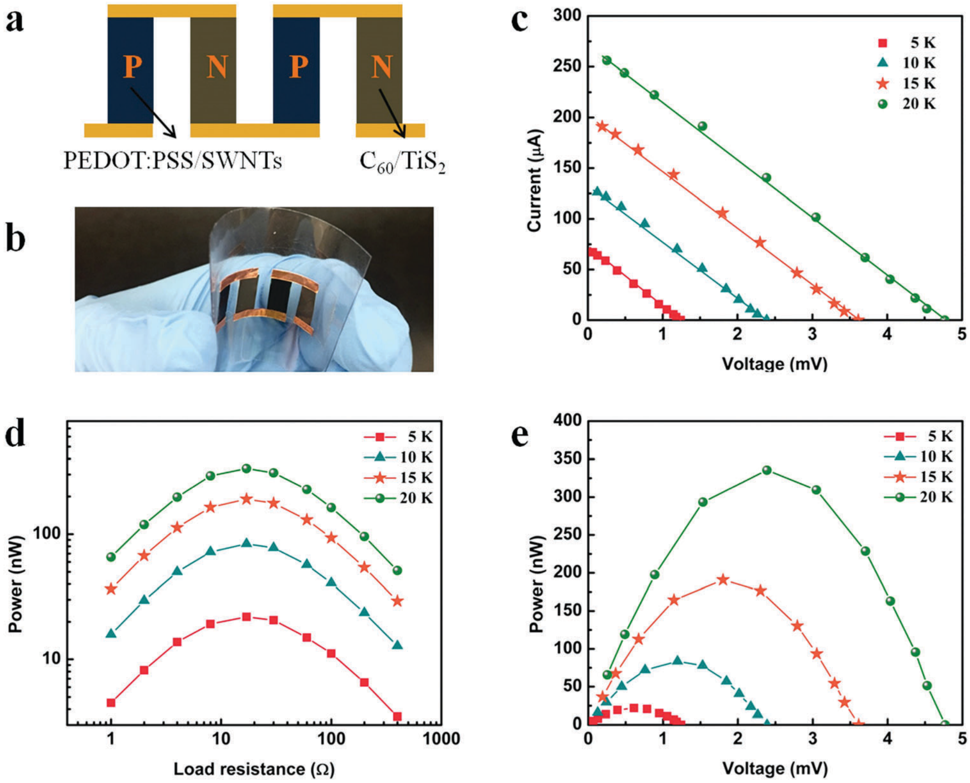

Fig. 7 Photograph and performance of the fabricated device. (a) Schematic illustration of the thermoelectric device consisting of 50 wt% SWNTs/PEDOT:PSS films (p-type legs) and 1 wt% C_{60}/TiS_2 hybrid films (n-type legs). (b) Corresponding photograph of the fabricated device with good flexibility. (c) The current–voltage curve of the device at different temperature differences. (d) The generated power of the device as a function of load resistance. (e) The power–voltage curve of the device at different temperature differences.

~4.8 mV at a temperature difference of 20 K. The output power (P) can be expressed as, $P = EI - I^2R_{in} = E^2R/(R + R_{in})^2$, where R is the load resistance. Therefore, the maximum output power can be obtained when the external load resistance matches the inner resistance of the device. As shown in Fig. 7d, output powers were plotted against the external load resistance. Under all the temperature gradients, the output powers reached the maximum when the load resistance was about 17 Ω, well matching the inner resistance of the device. In addition, the output powers were parabolic as a function of the output current (Fig. 7e). The maximum output power was about 335 nW at a temperature difference of 20 K. By dividing the cross-sectional area and the number of legs, the normalized maximum power density was 1.68 W m^{-2}, which is superior to those of the reported thermoelectric devices based on organic materials or organic/inorganic composites under a similar temperature difference.[6,13,18,35–37]

Conclusions

In summary, we demonstrate a facile approach to synthesize novel organic/inorganic heterostructures of C_{60}-intercalated TiS_2. Assembling 0D C_{60} nanoparticles onto 2D TiS_2 nanosheets not only significantly increased the Seebeck coefficient and the power factor, but also reduced the thermal conductivity of TiS_2. The resultant ZT was ~0.3 at 400 K, and comparable to that of the single crystal TiS_2 materials, which are very expensive, difficult to synthesize, and unsuitable for solution printing. This method can be extended to other TMDs for creating high-performance n-type thermoelectric materials. More importantly, the as-assembled organic/inorganic hybrid can serve as an ink for scalable printing of flexible and air-stable n-type legs in the thermoelectric devices. These results will significantly facilitate the utilization of thermoelectric devices in the field of flexible electronics.

Experimental

Materials

The pristine TiS_2 powders were synthesized *via* solid-state reaction by heating stoichiometric mixtures of Ti and S as reported in a previous paper.[39] *N*-Methyl-2-pyrrolidone (NMP), Isopropyl alcohol (IPA) and toluene were purchased from Sigma-Aldrich. C_{60} powders were purchased from Cheap Tubes Inc. PEDOT:PSS (PH 1000) was purchased from Clevios. All the materials were used as received.

Liquid assembly of C_{60}/TiS_2 nanosheet hybrids

For the fabrication process of the C_{60}/TiS_2 nanosheet hybrids, 0.2 g synthesized TiS_2 powders and 0.2 mL NMP were thoroughly mixed and manually ground with a pestle for 30 min. The powders were then transferred into a glass beaker with 40 mL IPA and ultra-sonicated in a bath sonicator for 3 h. Afterwards, the solution was centrifuged for 30 min at 4000 rpm twice to completely remove the bulk powders. The supernatant containing TiS_2 nanosheets was collected for further use. Various amounts (0.2 wt%, 0.5 wt%, 1 wt%, 2 wt%, 3 wt%, 5 wt%) of 1 mg mL^{-1} C_{60} toluene solution were then slowly added into the 30 mL 1 mg mL^{-1} TiS_2 nanosheet IPA solution, in order to deposit C_{60} onto the surface of the TiS_2 nanosheets. The mixture was further ultra-sonicated for 30 min to facilitate the surface deposition process.

Film preparation

The as-prepared solution containing the C_{60}/TiS_2 nanosheet hybrids can be printed onto substrates or vacuum filtered with filter membranes to obtain free-standing films. All the films were dried in a vacuum oven at 45 °C for 1 h to achieve the C_{60}/TiS_2 hybrid films. Then, the obtained C_{60}/TiS_2 hybrid films were annealed at 150 °C for 1 h, in order to remove the residual organic solvent molecules.

Device fabrication

p-Type ink was prepared by homogeneously dispersing 50 wt% SWNTs into PEDOT:PSS with a probe sonicator. A suspension containing 1 wt% C_{60}/TiS_2 hybrids was used as n-type ink. The flexible plastic substrate was treated with oxygen plasma for one hour before fabrication of the device. Both the p-type ink and n-type ink could be processed onto the plastic substrate with the desired patterns. Finally, the p-type legs and n-type legs were connected with conductive metals.

Characterization

The morphologies of the prepared TiS_2 nanosheets and C_{60}/TiS_2 hybrids were characterized by transmission electron microscopy (TEM, JEOL JEM-2010). The as-fabricated films were also characterized by atomic force microscopy (AFM, Bruker), X-ray diffraction (XRD, Bruker D8) with a Cu-K_α source (wavelength of 1.54056 Å), and a Raman spectrometer (Jobin-Yvon HORIBA LabRAM HR800 instrument coupled to an Olympus BX41 microscope, $\lambda_{exc.}$ = 514.5 nm). The film thickness was measured by using a Dektak profilometer. The electrical conductivity and Seebeck coefficient were measured along the in-plane direction at room temperature with home-built apparatus (see ESI†). The carrier concentration and mobility were measured according to the Hall effect in a Physics Property Measurements System (PPMS, Quantum Design). The high-temperature electrical conductivity and Seebeck coefficient of the films were measured with a ZEM-3 (ULVAC-RLKO). The mechanical flexibility was assessed by attaching the films on glass tubes with different diameters and testing their resistances as a function of tube radius. The in-plane thermal diffusivity (λ) of the film was tested by using a LFA 447 (Netzsch) with a special sample holder (Fig. S11, ESI†). The heat capacity (C_p) was measured using differential scanning calorimetry in the temperature range of 300–400 K. Then the thermal conductivity (κ) of the film was obtained from the relationship $\kappa = \rho\lambda C_p$ (ρ was the density). The out-of-plane thermal conductivity was also measured by using a LFA 447 for comparison. For the characterization of device performance, a temperature difference was produced by heating one side of the device with a resistance heater, and a voltage meter (Keithley 2182A) was used to record the generated thermoelectric voltage (Fig. S14, ESI†).

Conflicts of interest

The authors acknowledge no competing financial interests.

Acknowledgements

The authors appreciate the support from the startup funds of Texas A&M University and TEES, and also partial support from the National Science Foundation grant (CMMI 1634858). L. Fang also acknowledge the fund support form Qatar National Priority Research Program (NPRP9-160-2-088).

References

1 G. J. Snyder and E. S. Toberer, Complex thermoelectric materials, *Nat. Mater.*, 2008, **7**, 105–114.
2 Y. Du, S. Z. Shen, K. Cai and P. S. Casey, Research progress on polymer-inorganic thermoelectric nanocomposite materials, *Prog. Polym. Sci.*, 2012, **37**, 820–841.
3 Y. Zhou and L. D. Zhao, Promising thermoelectric bulk materials with 2D structures, *Adv. Mater.*, 2017, **29**, 1702676.
4 G. Tan, L. D. Zhao and M. G. Kanatzidis, Rationally designing high-performance bulk thermoelectric materials, *Chem. Rev.*, 2016, **116**, 12123–12149.
5 X. Zhang and L. D. Zhao, Thermoelectric materials: energy conversion between heat and electricity, *J. Materiomics*, 2015, **1**, 92–105.
6 O. Bubnova, *et al.*, Optimization of the thermoelectric figure of merit in the conducting polymer poly(3,4-ethylene-dioxythiophene), *Nat. Mater.*, 2011, **10**, 429–433.
7 G. H. Kim, L. Shao, K. Zhang and K. P. Pipe, Engineered doping of organic semiconductors for enhanced thermo-electric efficiency, *Nat. Mater.*, 2013, **12**, 719–723.
8 O. Bubnova, *et al.*, Semi-metallic polymers, *Nat. Mater.*, 2014, **13**, 190–194.
9 A. D. Avery, *et al.*, Tailored semiconducting carbon nano-tube networks with enhanced thermoelectric properties, *Nat. Energy*, 2016, **1**, 16033.
10 B. Russ, A. Glaudell, J. J. Urban, M. L. Chabinyc and R. A. Segalman, Organic thermoelectric materials for energy harvesting and temperature control, *Nat. Rev. Mater.*, 2016, **1**, 16050.
11 B. Russ, *et al.*, Power Factor Enhancement in Solution-Processed Organic n-type Thermoelectrics Through Molecular Design, *Adv. Mater.*, 2014, **26**, 3473–3477.

12 R. A. Schlitz, *et al.*, Solubility-Limited Extrinsic n-type Doping of a High Electron Mobility Polymer for Thermoelectric Applications, *Adv. Mater.*, 2014, **26**, 2825–2830.
13 Y. Sun, *et al.*, Organic Thermoelectric Materials and Devices Based on p- and n-Type poly(metal 1,1,2,2-ethenetetrathiolate)s, *Adv. Mater.*, 2012, **24**, 932–937.
14 Y. Sun, *et al.*, Flexible n-Type High-Performance Thermoelectric Thin Films of poly(nickel-ethylenetetrathiolate) Prepared by an Electrochemical Method, *Adv. Mater.*, 2016, **28**, 3351–3358.
15 C. L. Wan, *et al.*, Flexible n-type thermoelectric materials by organic intercalation of layered transition metal dichalcogenide TiS_2, *Nat. Mater.*, 2015, **14**, 622–627.
16 C. L. Wan, *et al.*, Dielectric Mismatch Mediates Carrier Mobility in Organic-Intercalated Layered TiS_2, *Nano Lett.*, 2015, **15**, 6302–6308.
17 C. L. Wan, *et al.*, Flexible thermoelectric foil for wearable energy harvesting, *Nano Energy*, 2016, **30**, 840–845.
18 R. M. Tian, *et al.*, A solution-processed TiS_2/organic hybrid superlattice film towards flexible thermoelectric devices, *J. Mater. Chem. A*, 2017, **5**, 564–570.
19 H. Imai, Y. Shimakawa and Y. Kubo, Large thermoelectric power factor in TiS_2 crystal with nearly stoichiometric composition, *Phys. Rev. B: Condens. Matter Mater. Phys.*, 2001, **64**, 241104.
20 R. Daou, *et al.*, Intrinsic effects of substitution and intercalation on thermal transport in two-dimensional TiS_2 single crystals, *J. Appl. Phys.*, 2015, **117**, 165101.
21 C. Wan, *et al.*, Ultrahigh thermoelectric power factor in flexible hybrid inorganic-organic superlattice, *Nat. Commun.*, 2017, **8**, 1024.
22 L. D. Hicks and M. S. Dresselhaus, Thermoelectric Figure of Merit of a One-Dimensional Conductor, *Phys. Rev. B: Condens. Matter Mater. Phys.*, 1993, **47**, 16631–16634.
23 L. D. Hicks and M. S. Dresselhaus, Effect of Quantum-Well Structures on the Thermoelectric Figure of Merit, *Phys. Rev. B: Condens. Matter Mater. Phys.*, 1993, **47**, 12727–12731.
24 L. D. Zhao, *et al.*, All-scale hierarchical thermoelectrics: MgTe in PbTe facilitates valence band convergence and suppresses bipolar thermal transport for high performance, *Energy Environ. Sci.*, 2013, **6**, 3346–3355.
25 K. Biswas, *et al.*, High-performance bulk thermoelectrics with all-scale hierarchical architectures, *Nature*, 2012, **489**, 414–418.
26 C. J. Vineis, A. Shakouri, A. Majumdar and M. G. Kanatzidis, Nanostructured Thermoelectrics: Big Efficiency Gains from Small Features, *Adv. Mater.*, 2010, **22**, 3970–3980.
27 Y. C. Lan, *et al.*, Structure Study of Bulk Nanograined Thermoelectric Bismuth Antimony Telluride, *Nano Lett.*, 2009, **9**, 1419–1422.
28 B. Poudel, *et al.*, High-thermoelectric performance of nanostructured bismuth antimony telluride bulk alloys, *Science*, 2008, **320**, 634–638.
29 Y. Ma, *et al.*, Enhanced thermoelectric figure-of-merit in p-type nanostructured bismuth antimony tellurium alloys made from elemental chunks, *Nano Lett.*, 2008, **8**, 2580–2584.
30 P.-A. Zong, *et al.*, Skutterudite with graphene-modified grain-boundary complexion enhances zT enabling high-efficiency thermoelectric device, *Energy Environ. Sci.*, 2017, **10**, 183–191.
31 R. Nunna, *et al.*, Ultrahigh thermoelectric performance in Cu_2Se-based hybrid materials with highly dispersed molecular CNTs, *Energy Environ. Sci.*, 2017, **10**, 1928–1935.
32 K. Zhang, Y. Zhang and S. R. Wang, Enhancing thermoelectric properties of organic composites through hierarchical nanostructures, *Sci. Rep.*, 2013, **3**, 3448.
33 M. Sumino, *et al.*, Thermoelectric properties of n-type C-60 thin films and their application in organic thermovoltaic devices, *Appl. Phys. Lett.*, 2011, **99**, 093308.
34 J. Paloheimo, H. Isotalo, J. Kastner and H. Kuzmany, Conduction mechanisms in undoped thin-films of c60 and c60/70, *Synth. Met.*, 1993, **56**, 3185–3190.
35 K. Suemori, S. Hoshino and T. Kamata, Flexible and lightweight thermoelectric generators composed of carbon nanotube-polystyrene composites printed on film substrate, *Appl. Phys. Lett.*, 2013, **103**, 153902.
36 K. Zhang, J. J. Qiu and S. R. Wang, Thermoelectric properties of PEDOT nanowire/PEDOT hybrids, *Nanoscale*, 2016, **8**, 8033–8041.
37 L. Wang, Q. Yao, W. Shi, S. Qu and L. Chen, Engineering carrier scattering at the interfaces in polyaniline based nanocomposites for high thermoelectric performances, *Mater. Chem. Front.*, 2017, **1**, 741–748.
38 C. J. Carmalt, S. A. O'Neill, I. P. Parkin and E. S. Peters, Titanium sulfide thin films from the aerosol-assisted chemical vapour deposition of $[Ti(SBut)_4]$, *J. Mater. Chem.*, 2004, **14**, 830–834.
39 L. Geng, *et al.*, Titanium Sulfides as Intercalation-Type Cathode Materials for Rechargeable Aluminum Batteries, *ACS Appl. Mater. Interfaces*, 2017, **9**, 21251–21257.
40 W. Sun, *et al.*, "Water-in-Salt" electrolyte enabled $LiMn_2O_4$/TiS_2 Lithium-ion batteries, *Electrochem. Commun.*, 2017, **82**, 71–74.
41 J. Yu, T. Ma, G. Liu and B. Cheng, Ehanced photocatalytic activity of bimodal mesoporous titania powders by C60 modification, *Dalton Trans.*, 2011, **40**, 6635–6644.
42 B. Chai, X. Liao, F. Song and H. Zhou, Fullerene modified C_3N_4 composites with enhanced photocatalytic activity under visible light irradiation, *Dalton Trans.*, 2014, **43**, 982–989.
43 J. Zhang, *et al.*, Thermoelectric properties of TiS_2-xPbSnSe$_3$ nanocomposites, *J. Alloys Compd.*, 2017, **696**, 1342–1348.
44 S. V. Faleev and F. Leonard, Theory of enhancement of thermoelectric properties of materials with nanoinclusions, *Phys. Rev. B: Condens. Matter Mater. Phys.*, 2008, **77**, 214304.
45 J. Y. Oh, *et al.*, Chemically exfoliated transition metal dichalcogenide nanosheet-based wearable thermoelectric generators, *Energy Environ. Sci.*, 2016, **9**, 1696–1705.
46 K. Jo, J. Choi and H. Kim, Benzyl viologen-assisted simultaneous exfoliation and n-doping of MoS_2 nanosheets via a solution process, *J. Mater. Chem. C*, 2017, **5**, 5395–5401.
47 Y. Ye, *et al.*, Enhanced thermoelectric performance of $xMoS_2$-TiS_2 nanocomposites, *J. Alloys Compd.*, 2016, **666**, 346–351.

48 E. Guilmeau, T. Barbier, A. Maignan and D. Chateigner, Thermoelectric anisotropy and texture of intercalated TiS_2, *Appl. Phys. Lett.*, 2017, **111**, 133903.
49 Y. Chen, *et al.*, Bendable n-Type Metallic Nanocomposites with Large Thermoelectric Power Factor, *Adv. Mater.*, 2017, **29**, 1604752.
50 W. Zhou, *et al.*, High-performance and compact-designed flexible thermoelectric modules enabled by a reticulate carbon nanotube architecture, *Nat. Commun.*, 2017, **8**, 14886.
51 Z. Zhang, J. Qiu and S. Wang, Roll-to-roll printing of flexible thin-film organic thermoelectric devices, *Manuf. Lett.*, 2016, **8**, 6–10.